PHYSICAL SCIENCES

Kinetic frustration by limited bond availability controls the LAT protein condensation phase transition on membranes

Simou Sun[1,2,3], Trevor GrandPre[4], David T. Limmer[1,5,6], Jay T. Groves[1,2,3,7]*

LAT is a membrane-linked scaffold protein that undergoes a phase transition to form a two-dimensional protein condensate on the membrane during T cell activation. Governed by tyrosine phosphorylation, LAT recruits various proteins that ultimately enable condensation through a percolation network of discrete and selective protein-protein interactions. Here, we describe detailed kinetic measurements of the phase transition, along with coarse-grained model simulations, that reveal that LAT condensation is kinetically frustrated by the availability of bonds to form the network. Unlike typical miscibility transitions in which compact domains may coexist at equilibrium, the LAT condensates are dynamically arrested in extended states, kinetically trapped out of equilibrium. Modeling identifies the structural basis for this kinetic arrest as the formation of spindle arrangements, favored by limited multivalent binding interactions along the flexible, intrinsically disordered LAT protein. These results reveal how local factors controlling the kinetics of LAT condensation enable formation of different, stable condensates, which may ultimately coexist within the cell.

INTRODUCTION

Protein condensates are emerging as one of the key organizational features in cell biology (*1*, *2*). Widely studied liquid condensates of proteins and nucleic acids are often described in terms of liquid-liquid phase separation (*1*, *3*, *4*). Recently, a distinct class of protein condensates, consisting of precisely regulated assemblies of signal transduction proteins on the membrane surface, have been identified (*5*–*8*). These two-dimensional (2D) condensates form through a multivalent bond percolation network of specific protein-protein interactions, a common motif of which is the modular binding interaction between Src Homology 2 (SH2) domains and phosphorylated tyrosine residues. The cross-linking protein-protein interactions are relatively strong (a few tens of k_BT) and occur through a limited number of specific binding sites (*9*–*11*). This limited bond availability establishes a distinct physical difference with the 3D protein–nucleic acid condensates, which are mediated through large numbers of weak interactions (*1*–*3*). Limited valency effects have been predicted to regulate cluster size and compactness (*12*, *13*), as well as to induce metastability in phase separations (*14*). Under physiological conditions in the living cell, selective kinase and phosphatase reactions regulate phosphorylation at the tyrosine binding sites and, in this way, govern the formation and dissolution of the 2D signaling protein condensates. Controlled tyrosine phosphorylation on scaffold and signaling proteins is a central feature of information processing within cellular signal transduction networks, positioning these membrane-associated condensates under direct control of signal transduction pathways (*5*–*8*).

Here, we describe studies of phase transition kinetics in a system consisting of linker for activation of T cells (LAT), growth factor receptor-bound protein 2 (Grb2), and Son of Sevenless (SOS). LAT is an intrinsically disordered, single-pass membrane anchored protein that, together with Grb2, SOS, and other molecules, serves as a hub for signal processing in the T cell receptor (TCR) signaling pathway (Fig. 1A) (*15*, *16*). LAT is a substrate for selective phosphorylation by the Zeta-chain-associated protein kinase 70 (Zap70) kinase in response to TCR activation by antigen (*17*). LAT has nine tyrosine sites, at least three of which can readily bind Grb2 through its SH2 domain when phosphorylated. Grb2 additionally has two SH3 domains, which can bind the proline-rich (PR) domain on SOS. SOS is capable of binding more than one Grb2 in this way and thus provides a cross-linking mechanism that leads to networked assembly of a LAT:Grb2:SOS protein condensate on the membrane surface (*5*, *7*). Other cross-linking interactions, such as a direct Grb2:Grb2 binding interface (*18*), may participate, but Grb2-mediated cross-linking is primarily limited to three LAT tyrosine sites, thus only achieving the minimum valency required for bond percolation. Another tyrosine site on LAT, which exhibits differential phosphorylation kinetics (*19*) and selectivity for the key signaling molecule phospholipase C-γ (PLC-γ) (*20*), provides a fourth cross-linking pathway that may be physiologically important in nucleation of the LAT condensate (*12*). Individually, the LAT:Grb2 and Grb2:SOS interactions exhibit relatively fast binding kinetics (*21*). However, rapid rebinding in the condensed state substantially extends the dwell time distribution for individual molecules and has been identified as a functional mechanism by which the condensate can control signaling output (*7*). The discrete binding interactions to specific sites, complex molecular kinetics, and intrinsic two-dimensionality suggest that LAT condensates are likely to exhibit very different material properties compared with 3D protein–nucleic acid condensates (*1*–*4*, *22*).

We reconstituted the LAT:Grb2:SOS system from purified components and performed detailed microscopic imaging studies tracking kinetics of the phase transition process on supported membranes. The results reveal that LAT:Grb2:SOS condensates undergo slow

[1]Department of Chemistry, University of California, Berkeley, Berkeley, CA 94720, USA. [2]California Institute for Quantitative Biosciences, University of California, Berkeley, Berkeley, CA 94720, USA. [3]Institute for Digital Molecular Analytics and Science, Nanyang Technological University, 639798 Singapore. [4]Department of Physics, University of California, Berkeley, Berkeley, CA 94720, USA. [5]Materials Science Division, Lawrence Berkeley National Laboratory, Berkeley, CA 94720, USA. [6]Chemical Science Division, Lawrence Berkeley National Laboratory, Berkeley, CA 94720, USA. [7]Division of Molecular Biophysics and Integrated Bioimaging, Lawrence Berkeley National Laboratory, Berkeley, CA 94720, USA.
*Corresponding author. Email: jtgroves@lbl.gov

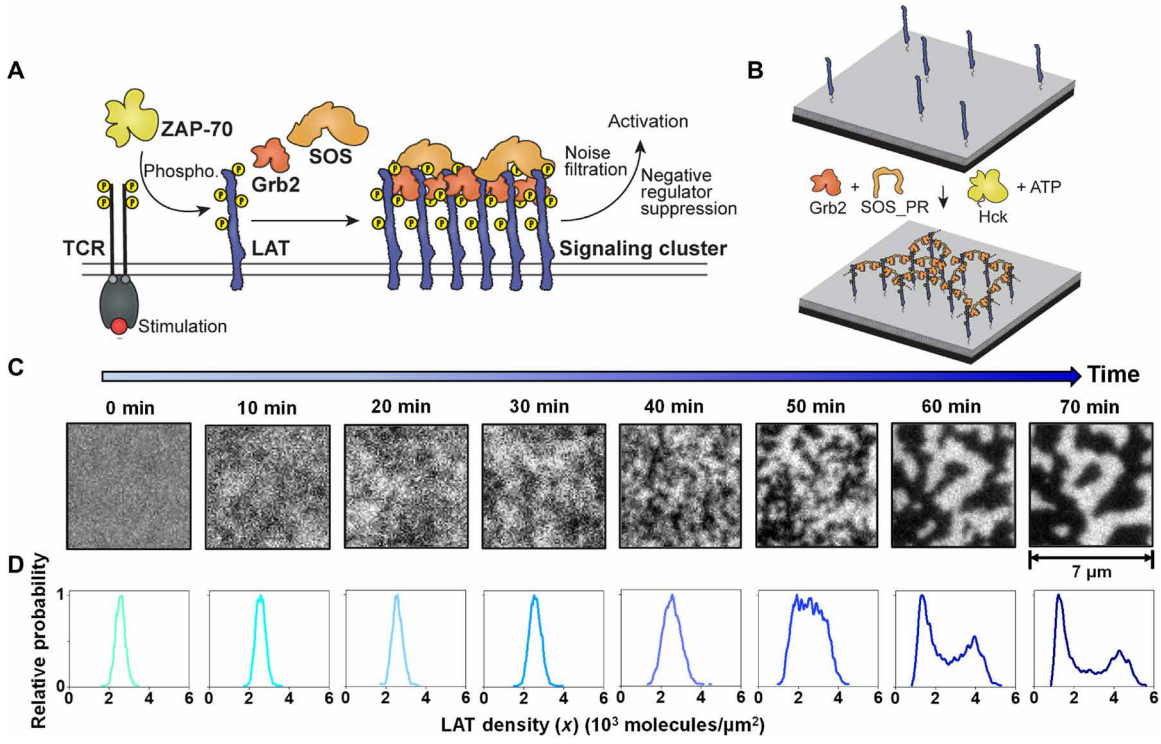

Fig. 1. Schematic illustration of the LAT:Grb2:SOS_PR condensation phase transition system. (**A**) The TCR signaling pathway, which involves assembly formation with LAT:Grb2:SOS. (**B**) In vitro reconstitution of the LAT:Grb2:SOS condensation phase transition on a supported lipid bilayer, where the assembly eventually relaxes to a disordered gel state. (**C**) TIRF images of the LAT-555 molecules during the progress of a phase transition with 5.8 μM Grb2 and 1.45 μM SOS_PR. (**D**) Corresponding LAT density (*x*) distribution over time. The density of LAT molecules was calculated on the basis of TIRF intensity and FCS readout calibration.

coarsening dynamics and kinetic arrest, preventing the condensate from reaching equilibrium. Temperature dependence of the phase transition kinetics, changes in molecular mobility, and the apparent final state composition exhibit signatures of a kinetically dominated control mechanism. We introduce a coarse-grained model of the LAT condensation based on the modular molecular binding kinetics, valency, and 2D mobility constraints that proved capable of recovering key experimental observations. The modeling reveals that limited valency and intrinsic flexibility of LAT favors the formation of spindle-like structures that act as kinetic traps, substantially slowing further equilibration of the system and leading to dynamic heterogeneity. We further discuss how insights from these experiments and modeling studies prompt some alternative interpretations of the mechanistic role of LAT and its condensation phase transition in T cell signaling.

RESULTS

The LAT protein condensation phase transition, which naturally occurs downstream of TCR signaling during T cell activation, can be reconstituted on supported lipid bilayers (SLBs) from purified proteins (Fig. 1, A and B) (*5*, *21*, *23*). Briefly, Alexa Fluor 555–labeled His_6-LAT (residues 27 to 233, LAT-555) was anchored on the SLB through Ni^{2+}-histidine chelation with Ni^{2+}-1,2-dioleoyl-sn-glycero-3-[(N-(5-amino-1-carboxypentyl)iminodiacetic acid)succinyl] (NTA-DOGS) lipid, doped into the membrane. Before condensation, LAT molecules were homogeneously distributed and diffused freely as monomers (D = 1.6 ± 0.3 μm²/s) on the membrane surface, as observed with total internal reflection fluorescence (TIRF) microscopy imaging and fluorescence correlation spectroscopy (FCS; fig. S1). In these studies, LAT is maintained in its phosphorylated state by the Src family kinase Hck, which is also tethered to the membrane and can phosphorylate LAT to completion (*21*). To initiate the condensation phase transition, phosphorylated LAT on the membrane was first allowed to incubate with Grb2 for 20 min, which enables binding of Grb2 to phosphorylated tyrosine sites on LAT to come to equilibrium. The concentration conditions used in these experiments are intentionally chosen such that Grb2 binding alone is insufficient to induce condensation and the LAT remains homogeneous (fig. S2). To trigger the phase transition, the PR domain of SOS (here simply referred to as SOS) was introduced to the Grb2 in solution. The SOS PR domain strongly cross-links Grb2, and this additional cross-linking controllably triggers the LAT:Grb2:SOS condensation (*5*, *7*, *21*). The three-component condensation occurs exclusively at the membrane surface; we observe no evidence of droplet formation of Grb2 and SOS in solution (fig. S3). After abrupt introduction of SOS, the ensuing LAT condensation phase transition is tracked through time using TIRF imaging (Fig. 1C).

The LAT:Grb2:SOS system undergoes a macroscopic phase transition to reach a steady state with two types of domains of drastically different LAT densities. Regions with high (bright) and low (dark) LAT concentration, defined as condensed and dispersed phases, respectively, are clearly visible. The condensed domains are quasi-stationary with stable and noncircular geometry, as well as with a broad range of sizes, and they exhibit constant local fluctuations at the edges (movie S1). No active [adenosine triphosphate

(ATP)–consuming] process is required to maintain the size and morphology of the condensed domains. In these experiments, the phase transitions occur over time scales of ~1 hour, but this time scale is related to the macroscopic size of the system, which involves molecular transport over many micrometers on the SLB. Over shorter length scales [e.g., a few hundred nanometers for some LAT condensates imaged in live T cells (*23*)], time scales will be substantially faster because the travel distance of LAT molecules is much shorter. We quantify the state of condensation by measuring the LAT surface density distribution on the membrane from the calibrated pixel brightness histogram of the fluorescence images (Fig. 1D; analysis details are provided in the Supplementary Materials and fig. S4). Each image pixel samples an area of ~9400 nm^2 on the membrane. Before condensation, the LAT density distribution is well fit by a single Gaussian peak with a narrow variance consistent with a random distribution of monomeric LAT. Over the course of the phase transition, the distribution broadens notably after an initial lag time and ultimately converges into two prominent and well-separated peaks (Fig. 1D).

We first characterize the final state under a variety of conditions to map the apparent LAT condensation phase diagram. To facilitate this analysis, the steady-state LAT density distributions were fit to two Gaussian peaks, the positions of which correspond to the average LAT density in the condensed and the dispersed phases (c_c and c_d; Fig. 2A). This fitting procedure was used to map the LAT density difference in the two phases across a variety of experimental temperatures to establish a phase diagram (detailed description of the analysis provided in the Supplementary Materials and fig. S5). For purposes of comparison, the phase coexistence boundary of a classical miscibility phase diagram driven by homotypic interactions is sketched in Fig. 2B. Although the LAT:Grb2:SOS system is technically driven by heterotypic interactions, there is generally an excess amount of Grb2 and SOS in solution such that a binding equilibrium with membrane-surface LAT is achieved without altering solution concentrations much. Thus, for fixed Grb2 and SOS concentrations in solution, LAT, Grb2, and SOS can be expected to maintain a constant stoichiometry on the membrane for each phase. Under these conditions, interactions between LAT molecules on the membrane (mediated through Grb2 and SOS) are effectively homotypic. For system compositions at temperatures below the phase coexistence line, condensed and dispersed phases coexist with compositions marked by the dashed tie lines. For equilibrium miscibility phase separation, these coexisting phase compositions correspond to thermodynamic free-energy minima and are fixed; varying initial protein concentrations leads to differing amounts of the two phases, but their compositions are preserved (*24*). The coexistence curve (or binodal) is indicated on Fig. 2B by the solid black line, identifying specific coexisting phase compositions at each temperature (highlighted with the horizontal dashed tie lines, for example). Generally, at higher temperatures, the coexisting phases become more similar in composition until the critical temperatures (T_c) are reached, above which the system remains macroscopically homogeneous.

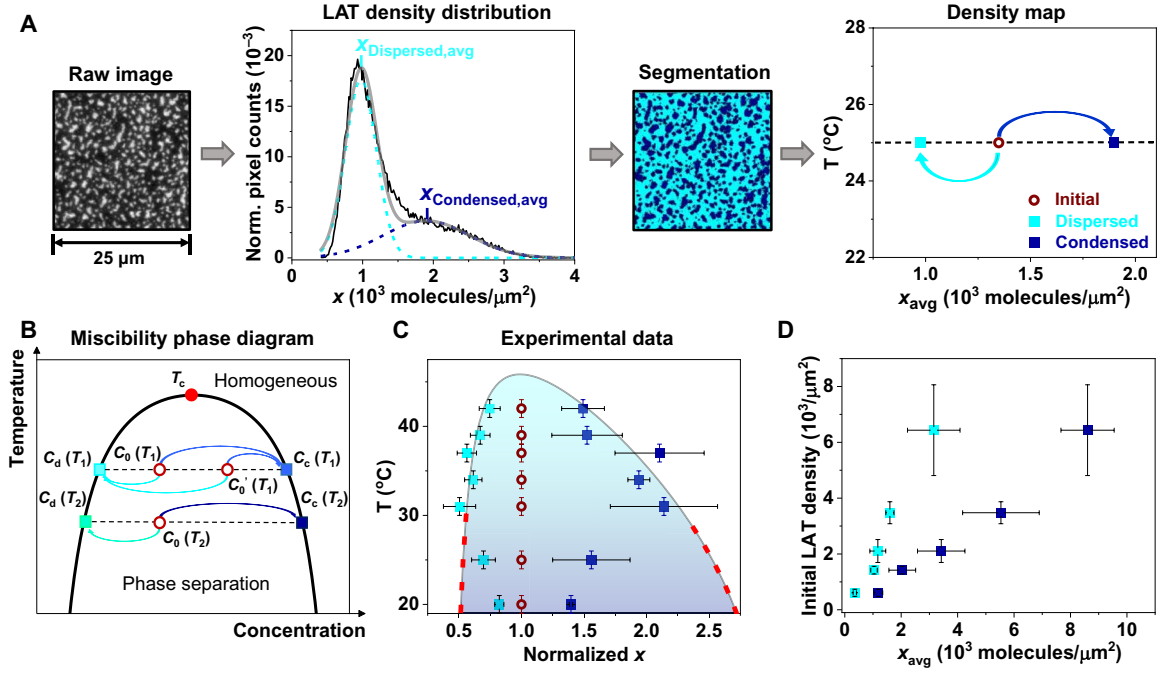

Fig. 2. Density map of the LAT:Grb2:SOS_PR system after the phase transition reaches the apparent final state. (**A**) Illustration of the analysis strategy to obtain the density map. The calibrated LAT density distribution from the raw image was fitted with two Gaussian peaks, the positions of which correspond to the average LAT densities in the dispersed and the condensed phases. Right: Representative density map at 25°C. Red open circle, initial LAT density before phase transition; royal blue solid square, average LAT density in the condensed phase; cyan solid square, average LAT density in the dispersed phase. (**B**) Demonstration of a classical miscibility phase diagram, where the condensed phase and the dispersed phase are in equilibrium. (**C**) Normalized average LAT density in the condensed domains and in the dispersed domains as a function of experimental temperature at an initial LAT density of 1200 ± 600 molecules/μm^2. The shaded area corresponds to the two-phase region of a modeled miscibility phase diagram. The red dashed lines on the binodal curve indicate deviation from the experimental data. (**D**) Average LAT density in the condensed and the dispersed phases plotted on the *x* axis with different initial LAT density plotted on the *y* axis.

The experimentally measured phase coexistence diagram for the LAT:Grb2:SOS condensation phase transition is shown in Fig. 2C. For temperatures closer to the physiological temperature (≥31°C), the coexisting phase compositions resemble a classic miscibility phase diagram. However, at lower temperatures, the experimental data deviate notably, with coexisting phases apparently much closer in composition. Whereas such behavior can be observed at equilibrium in systems with a lower critical point, this is unlikely to be the case for the LAT system because the demixing is purely driven by specific interprotein interactions (*25*–*27*); there are no direct interactions between LAT molecules, nor are there appreciable solvent effects. Instead, the observed slowed mobility within LAT condensates (*28*) indicates kinetic frustration as a probable cause of the observed behavior in this case. Furthermore, the 2D phase transition does not follow the classical tie-line principle with fixed c_c and c_d. Instead, LAT concentrations in the two phases grew correspondingly with increasing initial LAT concentrations (Fig. 2D), and the ratio of c_c to c_d, known as the partition coefficient (K) (*24*), remained constant (fig. S6). Both the compositions of coexisting phases and the breakdown of the tie-line principle suggest that the apparent final state of the LAT:Grb2:SOS phase transition is not an equilibrium free-energy minimum. Instead, it is likely kinetically and stably trapped in an out-of-equilibrium state.

We analyzed the kinetics of condensation by tracking the LAT surface density distribution over the course of the phase transition. The variance of this distribution, corresponding to the mean square LAT density fluctuation (with spatial sampling set by the ~9400-nm^2 image pixel size), provides a simple and monotonically increasing measure of the extent of phase separation. Kinetic traces of this parameter (normalized to 1.0 as the maximum variation achieved in the fully phase-separated state) measured for LAT:Grb2:SOS phase transitions at a variety of temperatures are plotted in Fig. 3A. The progress curves qualitatively exhibit a lag stage and a growth stage, independent of the initial LAT density (fig. S7), in which small and dynamic density fluctuations precede a macroscopic structural reorganization.

An empirical sigmoid model has been previously used to characterize similar behavior in the dynamics of kinetically controlled phase transitions of amyloid formation (*29*, *30*). From such analysis of the LAT transition kinetics, the principal parameters for the transition rate (k) and the lag time (t_{lag}) were extracted (Fig. 3B), where k characterizes the rate of the macroscopic structural rearrangement at t_{50} and t_{lag} represents the time delay between adding linker proteins to the start of the macroscopic phase transition (see Supplementary Materials for further discussion). Increasing temperature from 20° to 39°C progressively reduced an apparent kinetic bottleneck and sped up the phase transition, as quantified by increasing values of k and decreasing values of t_{lag} in the sigmoid model fits. This temperature dependence is counter to expectations from supersaturation-driven miscibility phase separation kinetics. In those cases, increasing temperature is expected to decrease the thermodynamic driving force for condensation and thus slow the rate of transition (*31*, *32*). Instead, the observed kinetic feature is reminiscent of the non-equilibrium phase transitions, such as gelation and glass transitions (*31*, *33*).

Over the 20° to 39°C temperature range, the LAT:Grb2:SOS phase transition exhibits Arrhenius kinetics with an activation energy $E_a \sim 31\ k_BT$ (Fig. 3C). This energy scale closely matches the estimated bonding energy between LAT molecules (see Supplementary Materials for details), which suggests that the phase transition is rate limited by bond formation and breakage. An additional feature in these results is that the phase transition kinetics exhibit a nonmonotonic dependence on temperature, with the fastest rate occurring at an intermediate temperature of 39°C. At the highest temperature measured (42°C, marked with asterisk in Fig. 3C), the kinetic barrier has largely been eliminated, but an attenuated thermodynamic driving force for phase separation could explain the observed decreased k and overall slower transition kinetics. Note that over the same range of temperature, there is negligible change in the unassembled LAT mobility (fig. S8); the diffusive mobility of LAT itself is likely not a major contributor to the phase transition kinetic behavior.

To investigate the microscopic structures within the protein network during the phase transition and maturation process, we conducted single-molecule tracking experiments on LAT. Briefly, 0.1 mole % (mol %) Alexa Fluor 488–labeled LAT (LAT-488) was doped into 99.9 mol % LAT-555, allowing visualization of both the macroscopic LAT configuration and individual molecular mobilities within. Four different stages of the macroscopic phase transition process, as depicted in Fig. 4A, were characterized: (i) before adding Grb2 and SOS_PR, (ii) the lag stage, (iii) the growth stage, and (iv) the apparent final state. Before any condensation, LAT exhibits

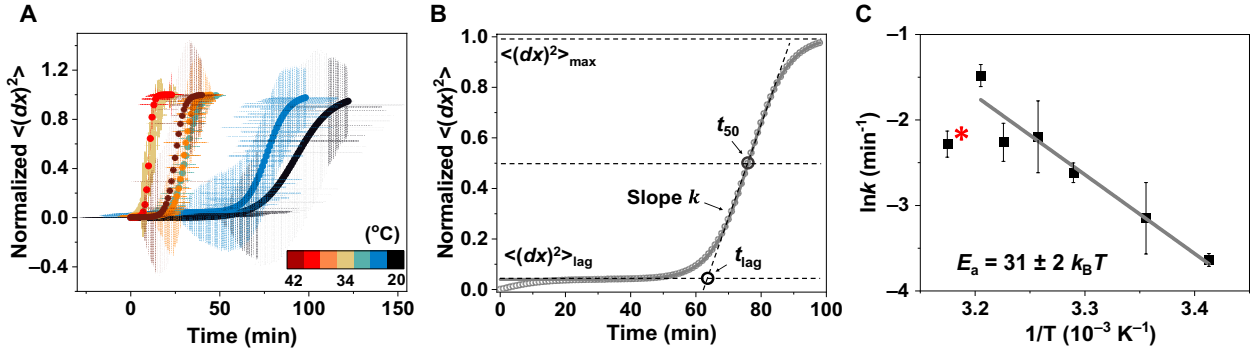

Fig. 3. Kinetic characterizations of the LAT:Grb2:SOS_PR condensation phase transition. (**A**) Normalized mean square LAT density fluctuation ($\langle\langle(dx)^2\rangle$) during the phase transition in a temperature range from 20° to 42°C. The data are color-coded according to the temperatures. Error bars represent SDs from at least three repeats of experiments at each temperature. (**B**) Illustration of the analysis strategy to extract the phase transition rate (k) and lag time (t_{lag}) by fitting the kinetic profile to a sigmoidal function. (**C**) k in log scale as a function of $1/T$ fitted to the Arrhenius equation (20° to 39°C; the fit did not include the 42°C data marked with asterisk), with a calculated $E_a = 31k_BT \pm 2k_BT$.

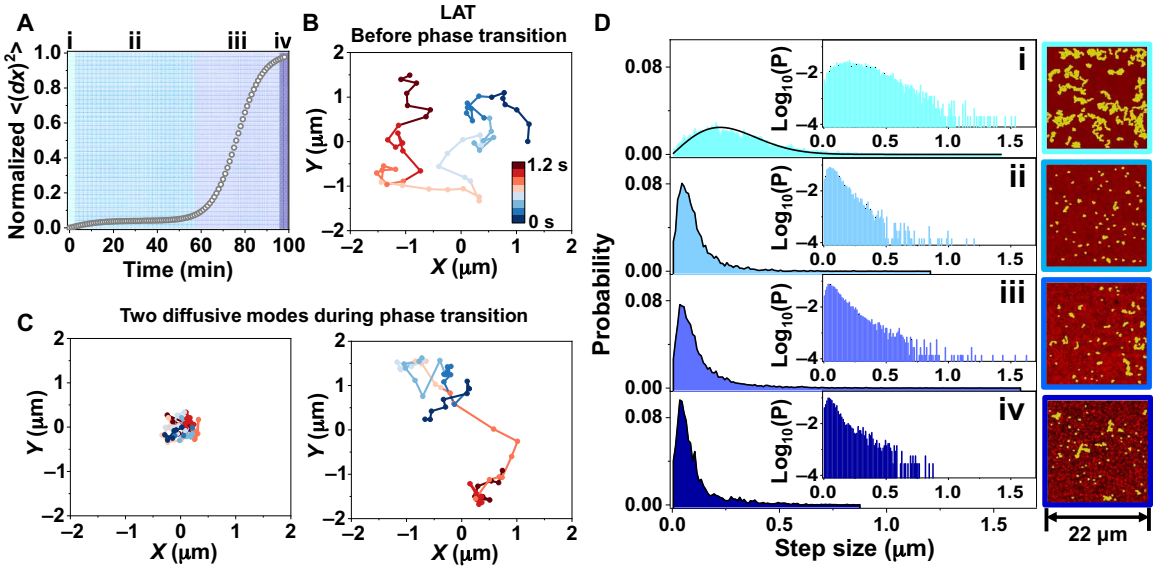

Fig. 4. Single-molecular dynamics during the LAT:Grb2:SOS_PR condensation phase transition. (**A**) Representative kinetic profile of the phase transition recorded on the 561-nm excitation channel (99.9 mol % LAT-555), with four different stages of the phase transition color-coded [(i) before phase transition, (ii) lag stage, (iii) growth stage, and (iv) apparent final state] for the single-molecule tracking experiments on the 488-nm excitation channel (0.1 mol % LAT-488). (**B** and **C**) Representative tracking trajectories of LAT-488 before phase transition and during phase transition, where LAT displayed at least two drastically different mobilities. The time axis is color-coded in the trajectories. (**D**) Step size distribution of the mobile LAT-488 molecules at the four stages and corresponding representative phase transition configurations (red color represents LAT-555) and tracking trajectories (yellow color represents LAT-488). Inset: Same step size distribution with probability plotted in log scale. The data in stage i was fitted to a single-component Rayleigh distribution. A total of 400 ± 100 molecules were tracked at 33 Hz for 100 frames to generate each distribution profile.

simple Brownian motion with diffusion coefficients of ~1.1 $\mu m^2/s$ (Fig. 4B). At later stages during the transition, a substantial amount of LAT exhibits highly trapped motion and some LAT exhibits intermediate frustrated motion (Fig. 4C).

In Fig. 4D, plots of measured LAT step size distributions during the four stages are displayed, along with the corresponding macroscopic phase transition images and single-molecule tracking trajectories. In stage i, the homogeneously distributed and unassembled LAT molecules displayed simple Brownian motion and are well fit by a Rayleigh distribution for single component diffusion. In stages ii, iii, and iv, the data shifts to smaller step sizes with most of the molecules being highly constrained and localized. The molecular motion is highly non-Brownian and a notable amount of heterogeneity exists. The largely reduced LAT mobility in the lag stage suggests that the LAT:Grb2:SOS bonding network readily formed oligomeric complexes early on. These structures are expected to contribute to the small LAT density fluctuations observed at the ensemble level, and they are kinetically stable possibly because of local valency saturation (*14*). In stage iii, unexpectedly, the LAT step size distribution broadened slightly. Despite the majority of LAT molecules still exhibiting trapped motion, we observed a small population of LAT with large step size compared to stage ii. This behavior is reminiscent of the fast-moving particles observed during a glass transition (*34*). This minor fast-moving population was observed to jump between two condensed domains, and it is potentially the major dynamic driving force for the macroscopic structural rearrangement during the slow coarsening process. In stage iv, the step size distribution narrowed down again. The number of LAT molecules in trapped states within condensates further increased. The LAT molecules observed in the dispersed phase within the tracking time scale displayed smaller step size than the freely diffusing LAT in stage i, possibly indicative of stably formed dimers or small oligomers. Note that two LAT molecules that are triply bound to each other will not readily form bonds with other LAT molecules because of limited valency and would be relatively stable as a free dimer.

To understand the slow coarsening kinetics accompanying LAT condensation, we have developed a simple coarse-grained model that encodes limited multivalency and 2D diffusion and explicitly examines spatial assembly. Prior modeling efforts on the LAT system have explored the LAT assembly dynamics as a function of bonding kinetics under homogeneous conditions (*35*, *36*) or used Brownian dynamics simulations of particles with rigid internal structure but without explicit kinetics of bond formation and breaking (*12*, *13*). We model membrane-bound monomer LAT molecules as diffusing in 2D with thermally driven Brownian motion. Each molecule excludes a volume with a characteristic diameter, σ, determined by the linear polymer's radius of gyration, which is estimated to be nearly σ = 10 nm and is implemented with a repulsive pair potential. Most of our studies are considered at a density of 1000 molecules/μm^2. We envision the bonding of a Grb2:SOS_PR:Grb2 complex to two adjacent LAT molecules as an effective first-order process, which is valid in the limit of a well-mixed solution phase and fast binding kinetics of SOS_PR:Grb2. The Grb2:SOS_PR:Grb2 linker is bound with an attempt rate k_B, with unbinding kinetics obeying detailed balance with respect to a bonding potential that includes a minimum bond energy, $-\overline{E}_b$, and is held at a rest length of 15 nm with a stiff harmonic potential (*37*, *38*). In addition, we impose a kinetic constraint that each LAT can form at most three bonds with other LAT molecules. The action of the linker is to bond LAT molecules together, colocalizing them in space. A phase diagram analogous to Fig. 2C is shown in fig. S9, in which, at elevated temperatures, LAT is found to be uniformly dispersed, while, at low temperatures, LAT

molecules assemble into a condensed gel that lacks long-range positional order consistent with experiments. The simulated phase diagram represents the system state after effectively infinite time and provides a theoretical comparison of what the system would look like if it were not dominated by kinetic frustration. The phase-separated temperature is set by the bond energy, and the disorder results from the formation of a network with sufficiently few mechanical constraints that there are many low-energy deformation modes.

The combination of diffusion and complex formation with limited LAT valency is sufficient to reproduce many of the experimental observations in Figs. 2 to 4. Specifically, we find an initially dispersed system when, quenched below, the phase separation transition temperature grows through a coarsening process in which an initial increase in LAT bonding occurs quickly and only over much longer time scales do isolated clusters aggregate. The initial bonding occurs with a characteristic time identified with the single complex formation rate, while the growth of large compact clusters occurs two orders of magnitude slower (Fig. 5A). Clusters grow as a power law in time with a growth exponent comparable with the experimental observations (Fig. 5A and fig. S10). At short times, the increase in the number of bonds occurs through the growth of many small clusters (Fig. 5D). The limited valency results in the formation of extended spindle-like structures at intermediate times. These mostly 1D connected strings of LAT molecules, which we here refer to as spindles, act as kinetic traps with long structural reorganization times. The intrinsic bond flexibility on LAT ensures that in the spindle structures, all but a few bonds are fully satisfied locally, limiting their ability to form a percolated network covering the 2D space. The spindle-like structures condense over time and display a metastable microphase where multiple aggregates exist. At the longest times, the system eventually forms a single large cluster, mediated by rare bond breaking events. The resulting gel exhibits large density fluctuations and a mean density far from close packed. The surface densities of LAT in the dense phase are in the range of 1900 to 3800 molecules/μm^2, comparable to the experimental observations as shown in Fig. 2C. The properties of the transient multidroplet system depend on the ratio of the rate of bond formation and the diffusion of LAT molecules (see a more detailed discussion about the steady-state properties in fig. S11).

We have characterized the dynamics within the condensed gel state and find that it exhibits remarkable dynamic heterogeneity. In Fig. 5B, the mean squared displacement is plotted as a function of time for a range of temperatures within the phase-separated region, which shows evidence of a broad range of time scales ranging from bond breaking on the shortest time scales to diffusive dynamics on the longest time scales. This observation aligns remarkably well with our previously reported LAT particle temporal transition from subdiffusive motion to normally diffusive motion in the LAT:Grb2:SOS condensates (*28*). Characteristic of many glassy systems, the relaxation of a single LAT molecule is non-Markovian with notable memory of its instantaneous local gel structure. This is evidenced by the decoupling of the distribution of relaxation times that we find for a LAT molecule conditioned on having just relaxed compared to its unconditioned distribution (Fig. 5C). These distinct dynamical processes result in slow reorganization, which manifests long coarsening times and have origins in the limited valency, and disordered gel structure (*39*).

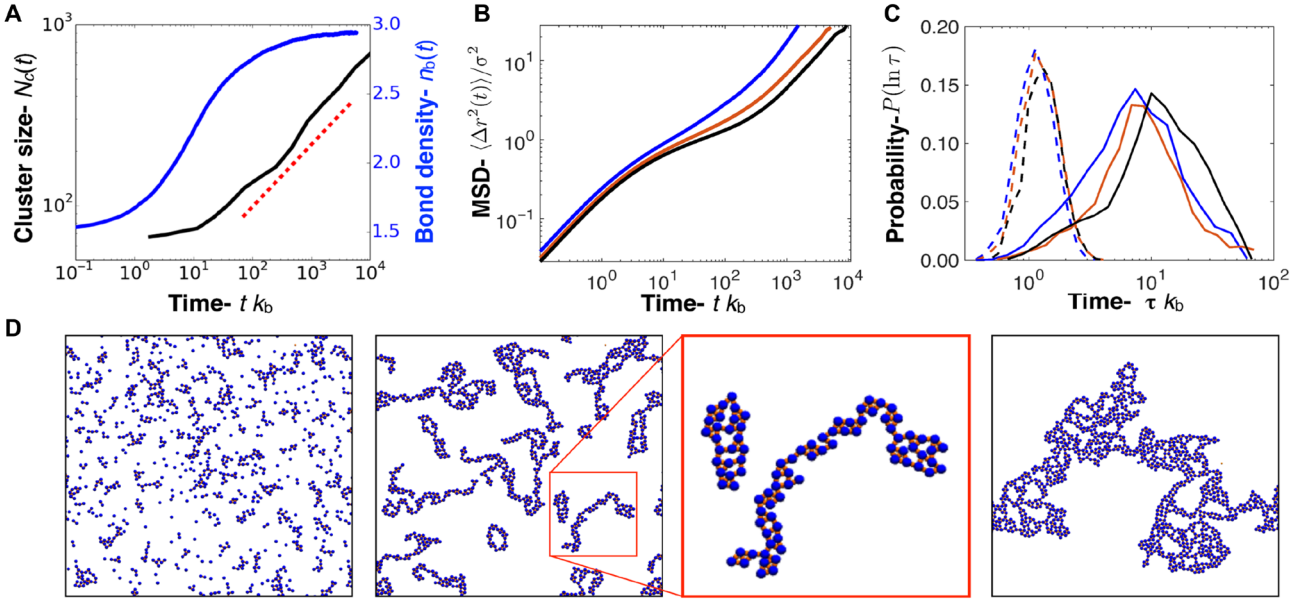

Fig. 5. Simulation results of LAT model. (**A**) The largest cluster size (black line) and average bonds (blue line) as a function of time, with comparison to a 1/3 coarsening power law (red dashed line) for a reduced density of $\rho\sigma^2 = 0.1$ and a reduced temperature of $k_BT/\bar{E}_b = 0.15$. (**B**) The mean squared displacement of the dense phase as a function of time showing caging effects that become more distinct with decreasing temperature for reduced temperatures of $k_BT/\bar{E}_b = 0.18$ (blue), 0.15 (red), and 0.14 (black) and reduced densities $\rho\sigma^2 = 0.27$, 0.32, and 0.36. (**C**) The distributions of persistence times (solid line), the time to move their particle diameter, σ, and exchange times (dashed line), the time to move another distance σ given that a LAT molecule has already moved that distance, for the same three temperatures and densities in (B). The lack of overlap demonstrates dynamic heterogeneity. (**D**) Typical trajectory of the coarse-grain model following aggregation for the system parameters plotted in (A) with the spindle structure shown in the red panel. Panels show configurations from the beginning, early, middle, and last times of the simulation, roughly times uniformly distributed along the logarithmic scale in (A).

DISCUSSION

Here, we have systematically characterized kinetic aspects of the membrane-localized LAT:Grb2:SOS condensation phase transition. The results reveal that the 2D phase transition and coexisting phase states differ notably from equilibrium miscibility phase separation; the LAT:Grb2:SOS phase transition is kinetically frustrated. With coarse-grained particle dynamics simulation, which includes only the two most fundamental physical properties of the experimental system, limited valency and 2D diffusion, we reproduced the experimental observations in the aspects of kinetic profile, coarsening dynamics, and dynamics within the condensates. Furthermore, modeling studies identified spindle-shaped configurations to present kinetic traps, and we observed dynamic heterogeneity in the condensed domains, which is a signature of glassy dynamics out of equilibrium. The modeling also enabled exploration of the experimentally unachievable equilibrium phase diagram (Fig. 2 and fig. S9), which confirmed that bonding kinetics can lead to simple binary phase separation when kinetic trapping is not a factor. A recent report has identified 3D protein droplets to form soft glassy materials with age-dependent properties (*40*). While the non-equilibrium features of this 3D system resemble some aspects of the 2D LAT system that we study here, there are also some important differences. Although the stable steady states of the LAT system exhibit highly trapped molecular movement of LAT on the membrane surface, they are not static. The Grb2 and SOS cross-linking molecules remain quite dynamic and exchange with solution molecules through binding and unbinding (*21*). This exchange leads to transient exposure of the underlying phosphorylated tyrosine residues on LAT, rendering them still accessible to phosphatases and kinases. Even in the condensed state, LAT molecules remain fully exposed to the solution and LAT condensates can be easily and quickly dissociated by the introduction of phosphatases at both low and high temperatures (fig. S12). The results in Fig. 2 (C and D) suggest that the arrested condensed phase is far from being fully packed, which is supported by observations from the simulation (Fig. 5D). This structural feature could partly be attributed to the dynamic conformational flexibility of the intrinsically disordered LAT protein.

LAT has long been known for its role as a molecular scaffold that brings together key signaling molecules once it is activated by phosphorylation on multiple tyrosine sites. Only recently has the ensuing assembly process been recognized as a type of protein condensation phase transition. The results that we describe here illustrate how the flexibility of LAT, along with limited valency and two dimensionality, leads to system behavior that is predominantly kinetically controlled. These observations contrast recently reported non-equilibrium phase separation behavior of P granules in the *Caenorhabditis elegans* embryo (*41*). In that system, the non-equilibrium behavior was driven by active cellular processes, while equilibrium thermodynamics remained the primary driving force on smaller length scales (100 nm). No active processes control the LAT:Grb2:SOS system dynamics, but its intrinsic restriction to the 2D membrane surface exacerbates kinetic traps, leading to non-equilibrium behavior due to kinetic frustration (*42*–*44*). In a biological setting, this suggests that the final state of a LAT condensate may be dominated by local conditions and signaling activity at the moment of its formation [for instance, kinetic competitions from other adaptor proteins (*15*), crowdedness of the local environment, etc.] more so than the overall molecular composition and state of the cell. The low valency of cross-linking interactions between LAT molecules, with predominantly just three available sites for Grb2 interactions, plays an important role limiting LAT condensation kinetics. A fourth phosphotyrosine site on LAT, which is highly selective for PLC-γ and only weakly binds Grb2, offers a fourth cross-linking possibility and has recently been reported to play an important role in stabilizing LAT condensation (*12*). PLC-γ is a critical signaling component in the TCR pathway that controls Ca^{2+} signaling and, ultimately, T cell activation (*15*, *19*). The results that we report here indicate that increased valency provided by PLC-γ recruitment could help break kinetic barriers limiting LAT condensation. This would ensure that LAT does not condense before PLC-γ arrival with potentially important consequences for coordinated signal timing (e.g., between the diverging downstream SOS and PLC-γ signaling pathways). There may also be conditions under which this type of kinetic limitation is overcome in other ways, resulting in differently composed LAT condensates. Overall, physical features of the LAT phase transition process introduce an additional angle for regulatory control and the possibility of multiple, distinct types of LAT condensate that may be able to coexist within a single cell.

MATERIALS AND METHODS

Chemicals

Dioleoylphosphatidylcholine (DOPC) and DOGS-NTA(Ni^{2+}) were purchased from Avanti Polar Lipids. Texas Red 1,2-dihexadecanoyl-*sn*-glycero-3-phosphoethanolamine (TR-DHPE) was purchased from Invitrogen. Alexa Fluor 555 maleimide dye and Alexa Fluor 488 maleimide dye were purchased from Life Technologies. Bovine serum albumin (BSA), (±)-6-hydroxy-2,5,7,8-tetramethylchromane-2-carboxylic acid (Trolox), catalase, 2-mercaptoethanol, $NiCl_2$, H_2SO_4, and ATP were purchased from Sigma-Aldrich. Glucose oxidase was purchased from Serva. Tris(2-carboxyethyl)phosphine (TCEP) was purchased from Thermo Scientific. Glucose and H_2O_2 were from Fisher Scientific. $MgCl_2$ was from EMD Chemicals. Tris-buffered saline (TBS) was purchased from Corning.

Protein purification and labeling

LAT, Grb2, and SOS_PR were purified similarly to previously published works (*7*, *9*, *21*). Human LAT cytosolic domain (residues 27 to 233, C117S) and full-length Grb2 were purified as described previously using an N-terminal 6-His tag, while the PR domain of SOS (residues 1051 to 1333) was purified with a similar strategy. For both Grb2 and SOS_PR, the N-terminal 6-His tag was removed with tobacco etch virus protease.

Protein was diluted to 50 μM, and Alexa Fluor dyes were prepared at 10 to 20 mM in anhydrous dimethyl sulfoxide. The protein was incubated with 5 mM TCEP on ice for 30 min to ensure that all cysteines were reduced. The dye was then added in one- to fivefold molar excess, depending on the percentage of labeling desired and the stability of the protein in the presence of the free dye. The proteins were then allowed to react with the dye for 2 hours on ice. The reaction was then quenched with 10 mM dithiothreitol for 10 min. Excess dye was removed by Superdex 75 column (10/300 GL, GE Healthcare). Percent labeling was calculated by measuring absorbance at peak excitation for the dye and 280 nm for the protein while taking into account the 280-nm contribution from the dye. Labeled protein was concentrated to the desired concentration, flash-frozen, and stored at −80°C.

Formation of functionalized supported lipid bilayers

Glass substrates (no. 1.5 thickness) were prepared by 10-min sonication in 1:1 isopropyl alcohol (IPA)/water mixture, 90-s microwave heating in water, 30 min soaking in 2 volume % Helamax solution and 5 min of piranha etching (H_2SO_4:H_2O_2 = 3:1 by volume), followed by excessive rinsing of H_2O (Milli-Q). The thus cleaned glass substrates were stored in Milli-Q water for no more than 3 days before using. The substrates were blow-dried with air before depositing vesicles to form SLBs.

Small unilamellar vesicles (SUVs) were prepared by mixing DOPC:Ni^{2+}-NTA-DOGS = 96:4 by molar percent in chloroform. If visualization of the bilayers was required, then an additional 0.005 mol % of TR-DHPE was added into the lipid composition. The solution mixture was then evaporated by a rotary evaporator for 15 min at 40°C. Lipid dried films were further blown with N_2 for another 15 min. The lipids were then resuspended in H_2O by vortexing, resulting in a concentration of about 1 mg/ml. Last, the vesicle solution was sonicated with a tip sonicator for 5 min with 20-s on and 50-s off cycles in an ice water bath. The membrane system was prepared on a flow chamber (μ-Slide, Ibidi) for experiments at and below 25°C. For experiments at temperatures higher than 25°C, the SLBs were formed in a polydimethylsiloxane ring attached to a round-glass coverslip, which were then brought into an incubator and incubated at the desired temperature. SLBs were formed on the glass substrate by incubating the SUVs mixed 1: 1 (v/v) with 2× TBS [10 mM Tris and 150 mM NaCl (pH 7.4)] for at least 30 min. The chambers were rinsed with 1× TBS buffer and then incubated with 100 mM $NiCl_2$ for 5 min. Next, BSA (1 mg/ml) was incubated for 10 min to block defects in supported membranes. Before protein incubation, the system was buffer-exchanged into protein dilution (PD) buffer containing 1× TBS, 5 mM $MgCl_2$, and 1 mM TCEP (pH 7.4). Proteins were centrifuged for 20 min at 4°C beforehand to remove possible aggregates. Depending on the desired density of the membrane proteins, LAT (50 to 500 nM) and Hck (15 nM) were incubated for 45 min to attach onto the bilayers via His-tag chemistry (*45*). The system was allowed to sit for another 20 min for unstably bound membrane proteins to dissociate from the surface. Between all incubation steps, the chambers were rinsed with PD buffer. All parts of the preparation were done at room temperature unless stated otherwise.

Microscopy

TIRF experiments were performed on a motorized inverted microscope (Nikon Eclipse Ti-E, Technical Instruments, Burlingame, CA) equipped with a motorized Epi/TIRF illuminator, motorized Intensilight mercury lamp (Nikon C-HGFIE), Perfect Focus system, and a motorized stage (MS-2000, Applied Scientific Instrumentation, Eugene, OR). A laser launch with 488- and 561-nm (Coherent OBIS, Santa Clara, CA) diode lasers was controlled by an OBIS Scientific Remote (Coherent Inc., Santa Clara, CA) and aligned into a fiber launch custom-built by Solamere Technology Group Inc. (Salt Lake City, UT). The optical path was then aligned to a 100× 1.49–numerical aperture oil immersion TIRF objective (Nikon). A dichroic beamsplitter (ZT405/488/561/640rpc, Chroma Technology Corp., Bellows Falls, VT) reflected the laser light through the objective lens, and fluorescence images were recorded using an electron-multiplying charge-coupled device (iXon 897DU, Andor Inc., South Windsor, CT) after passing through a laser-blocking filter (ZET405/488/561/640m-TRF, Chroma Technology Corp., Bellows Falls, VT). Laser powers measured at the sample were approximately 8 mW for the 488-nm channel when taking the single-molecule tracking measurements. All acquisitions were obtained using Micro-Manager. A Transistor–transistor logic (TTL) signal from the appropriate laser triggered the camera exposure.

Single-particle tracking

All analyses were performed on the central region of the images with radius of 160 pixels to minimize uneven illumination. Particle identification and particle tracking routines were performed using Trackmate. A single particle was identified and detected by a segmenter on the basis of an approximation of the Laplacian of Gaussian operator by difference of Gaussian, with subpixel localization and an estimated particle diameter of 0.6 μm. An initial quality thresholding was performed before tracking analysis to ensure optimized single-particle density, which, in this case, is 0.07 to 0.1 molecules/μm^2. Particle diffusion was tracked by the Linear Assignment Problem tracker, with the maximum travel distance of 16 pixels per frame at a frame rate of 33 Hz and maximum frame gap of two frames. All results were inspected to verify proper particle connection, and only tracks displaying more than five spots are processed for further analysis.

Simulation methods

Each LAT molecule is treated as a disk with a diameter of σ = 10 nm based on the radius of gyration. The dynamics of the *i*th LAT follows an overdamped Langevin equation of the form

$$\dot{\boldsymbol{r}}_i = \mu \boldsymbol{F}_i(\boldsymbol{r}^N) + \sqrt{2 k_B T \mu}\, \eta_i \tag{1}$$

where k_B is Boltzmann constant, μ is the single particle mobility, and T is the temperature of the system, and combined, they set the temperature-dependent diffusion by the fluctuation-dissipation relation in the dilute limit, $D = k_B T \mu$. The interactions, $\boldsymbol{F}_i(\boldsymbol{r}^N) = -\nabla_i U(\boldsymbol{r}^N)$, are conservative, pairwise additive, and, in general, depend on the coordinates of all N particles in the system represented by configuration $\boldsymbol{r}^N$. The statistics of η_i are zero on average, $\langle \eta_i^\alpha(t) \rangle = 0$, and have a variance that is delta correlated in time, $\langle \eta_i^\alpha(t)\, \eta_j^\beta(t') \rangle = \delta_{ij} \delta_{\alpha,\beta} \delta(t - t')$, for the α and β components of the random force, which correspond to the x and y dimensions. In practice, the mobility and k_B are set to unity and the dynamics generated a first-order Euler method with Ito time discretization. We consider conservative pairwise forces with excluded area given by the Weeks-Chandler-Anderson potential (*46*)

$$U_{WCA}(r) = \begin{cases} 4\epsilon\left[\left(\frac{\sigma}{r}\right)^{12} - \left(\frac{\sigma}{r}\right)^{6}\right] + \epsilon & r \le 2^{1/6}\sigma \\ 0 \quad \text{otherwise} \end{cases} \tag{2}$$

with a characteristic energy scale ϵ = 1. Bonded LAT molecules also have a pairwise bond force with other LAT molecules given by a harmonic potential

$$E_b(r) = \frac{1}{2}\kappa (r - 1.5\sigma)^2 - \bar{E}_b \tag{3}$$

where $\bar{E}_b$ is set to 4ϵ. A given LAT can at most be bound to three other LAT molecules, but the number of bonds at a given time is a dynamic quantity because we allow for bonds to be made and broken. Bonds between pairs of LAT are formed and broken with the Metropolis-Hastings algorithm with an energy change to make a bond given by $E_b(r)$ and to break a bond given by $-E_b(r)$ (*47*, *48*). A bond

is made at rate $k_{b,r}$ when two LAT molecules are within a reactive distance of 2σ and have less than three bonds. A bond is broken with rate $k_{u,r}$ given that the pair of LAT molecules are within a reactive distance of $r_c = 2\sigma$. The rates are related to each other by a detailed balance relation

$$\frac{k_{b,r}}{k_{u,r}} = e^{-\beta E_b(r)} \quad (4)$$

with

$$k_{b,r} = k_b[1 - \Theta(r - r_c)] \quad (5)$$

Here, k_b is the prefactor rate that sets the time scale of the kinetics and $\Theta(r - r_c)$ is a Heaviside function that enforces that only when particles are within a reactive distance are they capable of forming a bond. To ensure realistic dynamics, we choose a tight spring constant of $\kappa = 80\epsilon/\sigma^2$ to avoid bound LAT extending beyond the reactive distance. The simulation code used can be found at Zenodo (https://zenodo.org/badge/latestdoi/426642312).

SUPPLEMENTARY MATERIALS

Supplementary material for this article is available at https://science.org/doi/10.1126/sciadv.abo5295

REFERENCES AND NOTES

1. A. A. Hyman, C. A. Weber, F. Jülicher, Liquid-liquid phase separation in biology. *Annu. Rev. Cell Dev. Biol.* **30**, 39–58 (2014).
2. S. F. Banani, H. O. Lee, A. A. Hyman, M. K. Rosen, Biomolecular condensates: Organizers of cellular biochemistry. *Nat. Rev. Mol. Cell Biol.* **18**, 285–298 (2017).
3. J. Berry, C. P. Brangwynne, M. Haataja, Physical principles of intracellular organization via active and passive phase transitions. *Rep. Prog. Phys.* **81**, 046601 (2018).
4. S. Alberti, A. Gladfelter, T. Mittag, Considerations and challenges in studying liquid-liquid phase separation and biomolecular condensates. *Cell* **176**, 419–434 (2019).
5. X. Su, J. A. Ditlev, E. Hui, W. Xing, S. Banjade, J. Okrut, D. S. King, J. Taunton, M. K. Rosen, R. D. Vale, Phase separation of signaling molecules promotes T cell receptor signal transduction. *Science* **352**, 595–599 (2016).
6. L. B. Case, X. Zhang, J. A. Ditlev, M. K. Rosen, Stoichiometry controls activity of phase-separated clusters of actin signaling proteins. *Science* **363**, 1093–1097 (2019).
7. W. Y. C. Huang, S. Alvarez, Y. Kondo, Y. K. Lee, J. K. Chung, H. Y. M. Lam, K. H. Biswas, J. Kuriyan, J. T. Groves, A molecular assembly phase transition and kinetic proofreading modulate Ras activation by SOS. *Science* **363**, 1098–1103 (2019).
8. S. Banjade, M. K. Rosen, Phase transitions of multivalent proteins can promote clustering of membrane receptors. *eLife* **3**, e04123 (2014).
9. W. Y. C. Huang, J. A. Ditlev, H.-K. Chiang, M. K. Rosen, J. T. Groves, Allosteric modulation of Grb2 recruitment to the intrinsically disordered scaffold protein, LAT, by remote site phosphorylation. *J. Am. Chem. Soc.* **139**, 18009–18015 (2017).
10. J. A. Simon, S. L. Schreiber, Grb2 SH3 binding to peptides from SOS: Evaluation of a general model for SH3-ligand interactions. *Chem. Biol.* **2**, 53–60 (1995).
11. T.-J. Liao, H. Jang, R. Nussinov, D. Fushman, High-affinity interactions of the nSH3/cSH3 domains of Grb2 with the C-terminal proline-rich domain of SOS1. *J. Am. Chem. Soc.* **142**, 7, 3401–3411 (2020).
12. L. Zeng, I. Palaia, A. Šarić, X. Su, PLCγ1 promotes phase separation of T cell signaling components. *J. Cell Biol.* **220**, e202009154 (2021).
13. I. Palaia, A. Šarić, Controlling cluster size in 2D phase-separating binary mixtures with specific interactions. *J. Chem. Phys.* **156**, 194902 (2022).
14. S. Ranganathan, E. I. Shakhnovich, Dynamic metastable long-living droplets formed by sticker-spacer proteins. *eLife* **9**, e56159 (2020).
15. A. H. Courtney, W.-L. Lo, A. Weiss, TCR signaling: Mechanisms of initiation and propagation. *Trends Biochem. Sci.* **43**, 108–123 (2018).
16. L. Balagopalan, R. L. Kortum, N. P. Coussens, V. A. Barr, L. E. Samelson, The linker for activation of T cells (LAT) signaling hub: from signaling complexes to microclusters. *J. Biol. Chem.* **290**, 26422–26429 (2015).
17. N. H. Shah, Q. Wang, Q. Yan, D. Karandur, T. A. Kadlecek, I. R. Fallahee, W. P. Russ, R. Ranganathan, A. Weiss, J. Kuriyan, An electrostatic selection mechanism controls sequential kinase signaling downstream of the T cell receptor. *eLife* **5**, e20105 (2016).
18. C.-W. Lin, L. M. Nocka, B. L. Stinger, J. B. DeGrandchamp, L. J. N. Lew, S. Alvarez, H. T. Phan, Y. Kondo, J. Kuriyan, J. T. Groves, A two-component protein condensate of the EGFR cytoplasmic tail and Grb2 regulates Ras activation by SOS at the membrane. *Proc. Natl. Acad. Sci. U.S.A.* **119**, e2122531119 (2022).
19. W.-L. Lo, N. H. Shah, S. A. Rubin, W. Zhang, V. Horkova, I. R. Fallahee, O. Stepanek, L. I. Zon, J. Kuriyan, A. Weiss, Slow phosphorylation of a tyrosine residue in LAT optimizes T cell ligand discrimination. *Nat. Immunol.* **20**, 1481–1493 (2019).
20. W. Zhang, R. P. Trible, M. Zhu, S. K. Liu, C. J. McGlade, L. E. Samelson, Association of Grb2, Gads, and phospholipase C-γ1 with phosphorylated LAT tyrosine residues. *J. Biol. Chem.* **275**, 23355–23361 (2000).
21. W. Y. C. Huang, Q. Yan, W.-C. Lin, J. K. Chung, S. D. Hansen, S. M. Christensen, H.-L. Tu, J. Kuriyan, J. T. Groves, Phosphotyrosine-mediated LAT assembly on membranes drives kinetic bifurcation in recruitment dynamics of the Ras activator SOS. *Proc. Natl. Acad. Sci. U.S.A.* **113**, 8218–8223 (2016).
22. A. S. Lyon, W. B. Peeples, M. K. Rosen, A framework for understanding the functions of biomolecular condensates across scales. *Nat. Rev. Mol. Cell Biol.* **22**, 215–235 (2021).
23. D. B. McAffee, M. K. O'Dair, J. J. Lin, S. T. Low-Nam, K. B. Wilhelm, S. Kim, S. Morita, J. T. Groves, Discrete LAT condensates encode antigen information from single pMHC:TCR binding events. bioRxiv 2021.12.16.472676 [Preprint]. 16 December 2021; https://doi.org/10.1101/2021.12.16.472676.
24. J. A. Riback, L. Zhu, M. C. Ferrolino, M. Tolbert, D. M. Mitrea, D. W. Sanders, M.-T. Wei, R. W. Kriwacki, C. P. Brangwynne, Composition-dependent thermodynamics of intracellular phase separation. *Nature* **581**, 209–214 (2020).
25. G. L. Dignon, W. Zheng, Y. C. Kim, J. Mittal, Temperature-controlled liquid–liquid phase separation of disordered proteins. *ACS Cent. Sci.* **5**, 821–830 (2019).
26. H. Falahati, A. Haji-Akbari, Thermodynamically driven assemblies and liquid–liquid phase separations in biology. *Soft Matter* **15**, 1135–1154 (2019).
27. H. Jiang, S. Wang, Y. Huang, X. He, H. Cui, X. Zhu, Y. Zheng, Phase transition of spindle-associated protein regulate spindle apparatus assembly. *Cell* **163**, 108–122 (2015).
28. W. Y. C. Huang, H.-K. Chiang, J. T. Groves, Dynamic scaling analysis of molecular motion within the LAT:Grb2:SOS protein network on membranes. *Biophys. J.* **113**, 1807–1813 (2017).
29. W.-F. Xue, S. W. Homans, S. E. Radford, Systematic analysis of nucleation-dependent polymerization reveals new insights into the mechanism of amyloid self-assembly. *Proc. Natl. Acad. Sci. U.S.A.* **105**, 8926–8931 (2008).
30. A. L. Serrano, J. P. Lomont, L.-H. Tu, D. P. Raleigh, M. T. Zanni, A free energy barrier caused by the refolding of an oligomeric intermediate controls the lag time of amyloid formation by hIAPP. *J. Am. Chem. Soc.* **139**, 16748–16758 (2017).
31. B. A. Rogers, K. B. Rembert, M. F. Poyton, H. I. Okur, A. R. Kale, T. Yang, J. Zhang, P. S. Cremer, A stepwise mechanism for aqueous two-phase system formation in concentrated antibody solutions. *Proc. Natl. Acad. Sci. U.S.A.* **116**, 15784–15791 (2019).
32. O. Galkin, P. G. Vekilov, Control of protein crystal nucleation around the metastable liquid-liquid phase boundary. *Proc. Natl. Acad. Sci. U.S.A.* **97**, 6277–6281 (2000).
33. Y. S. Elmatad, D. Chandler, J. P. Garrahan, Corresponding states of structural glass formers. *J. Phys. Chem. B* **113**, 5563–5567 (2009).
34. E. R. Weeks, J. C. Crocker, A. C. Levitt, A. Schofield, D. A. Weitz, Three-dimensional direct imaging of structural relaxation near the colloidal glass transition. *Science* **287**, 627–631 (2000).
35. A. Nag, M. I. Monine, J. R. Faeder, B. Goldstein, Aggregation of membrane proteins by cytosolic cross-linkers: theory and simulation of the LAT-Grb2-SOS1 system. *Biophys. J.* **96**, 2604–2623 (2009).
36. A. Nag, M. Monine, A. S. Perelson, B. Goldstein, Modeling and simulation of aggregation of membrane protein LAT with molecular variability in the number of binding sites for cytosolic Grb2-SOS1-Grb2. *PLOS ONE* **7**, e28758 (2012).
37. C.-C. Lin, F. A. Melo, R. Ghosh, K. M. Suen, L. J. Stagg, J. Kirkpatrick, S. T. Arold, Z. Ahmed, J. E. Ladbury, Inhibition of basal FGF receptor signaling by dimeric Grb2. *Cell* **149**, 1514–1524 (2012).
38. C. B. McDonald, V. Bhat, D. Kurouski, D. C. Mikles, B. J. Deegan, K. L. Seldeen, I. K. Lednev, A. Farooq, Structural landscape of the proline-rich domain of Sos1 nucleotide exchange factor. *Biophys. Chem* **175–176**, 54–62 (2013).
39. L. O. Hedges, L. Maibaum, D. Chandler, J. P. Garrahan, Decoupling of exchange and persistence times in atomistic models of glass formers. *J. Chem. Phys.* **127**, 211101 (2007).
40. L. Jawerth, E. Fischer-Friedrich, S. Saha, J. Wang, T. Franzmann, X. Zhang, J. Sachweh, M. Ruer, M. Ijavi, S. Saha, J. Mahamid, A. A. Hyman, F. Jülicher, Protein condensates as aging Maxwell fluids. *Science* **370**, 1317–1323 (2020).
41. A. W. Fritsch, A. F. Diaz-Delgadillo, O. Adame-Arana, C. Hoege, M. Mittasch, M. Kreysing, M. Leaver, A. A. Hyman, F. Jülicher, C. A. Weber, Local thermodynamics govern formation

and dissolution of *Caenorhabditis elegans* P granule condensates. *Proc. Natl. Acad. Sci. U.S.A.* **118**, e2102772118 (2021).
42. P. J. Lu, E. Zaccarelli, F. Ciulla, A. B. Schofield, F. Sciortino, D. A. Weitz, Gelation of particles with short-range attraction. *Nature* **453**, 499–503 (2008).
43. V. Trappe, V. Prasad, L. Cipelletti, P. N. Segre, D. A. Weitz, Jamming phase diagram for attractive particles. *Nature* **411**, 772–775 (2001).
44. F. Cardinaux, T. Gibaud, A. Stradner, P. Schurtenberger, Interplay between spinodal decomposition and glass formation in proteins exhibiting short-range attractions. *Phys. Rev. Lett.* **99**, 118301 (2007).
45. J. A. Nye, J. T. Groves, Kinetic control of histidine-tagged protein surface density on supported lipid bilayers. *Langmuir* **24**, 4145–4149 (2008).
46. J. D. Weeks, D. Chandler, H. C. Andersen, Role of repulsive forces in determining the equilibrium structure of simple liquids. *J. Chem. Phys.* **54**, 5237–5247 (1971).
47. D. Frenkel, B. Smit, *Understanding Molecular Simulation: From Algorithms to Applications* (Elsevier, Ed. 2, 2001), vol. 1.
48. C. Fröhner, F. Noé, Reversible interacting-particle reaction dynamics. *J. Phys. Chem. B* **122**, 11240–11250 (2018).

Acknowledgments: We thank L. B. Nocka, L. J. N. Lew, A. A. Lee, K. B. Wilhelm, and J. B. DeGrandchamp for sharing reagents and helpful discussions. **Funding:** This work was supported by the Novo Nordisk Foundation Challenge Program under the Center for Geometrically Engineered Cellular Systems. Additional support was provided by NIH grant PO1 A1091580. T.G. and D.T.L were supported by the NSF, Division of Chemistry award no. NSF grant CHE1954580. **Author contributions:** S.S. and J.T.G. conceived the study. S.S. designed and performed the experiments and analyzed the experimental data. T.G. and D.T.L. developed a model, ran simulations, and analyzed the data from it. S.S., T.G., D.T.L., and J.T.G. wrote the manuscript. **Competing interests:** The authors declare that they have no competing interests. **Data and materials availability:** All data needed to evaluate the conclusions in the paper are present in the paper and/or the Supplementary Materials.

Submitted 10 February 2022
Accepted 13 September 2022
Published 2 November 2022
10.1126/sciadv.abo5295

ScienceAdvances

Kinetic frustration by limited bond availability controls the LAT protein condensation phase transition on membranes

Simou Sun, Trevor GrandPre, David T. Limmer, and Jay T. Groves

Sci. Adv., **8** (44), eabo5295.
DOI: 10.1126/sciadv.abo5295

Science Advances (ISSN) is published by the American Association for the Advancement of Science. 1200 New York Avenue NW, Washington, DC 20005. The title *Science Advances* is a registered trademark of AAAS.